THE LARGE SKY AREA MULTI-OBJECT FIBER SPECTROSCOPIC TELESCOPE QUASAR SURVEY: QUASAR PROPERTIES FROM THE FIRST DATA RELEASE

Y. L. Ai[1,2], Xue-Bing Wu[1,3], Jinyi Yang[1,3], Qian Yang[1,3], Feige Wang[1,3], Rui Guo[1,3], Wenwen Zuo[4], Xiaoyi Dong[1],
Y.-X. Zhang[5], H.-L. Yuan[5], Y.-H. Song[5], Jianguo Wang[6,7], Xiaobo Dong[6,7], M. Yang[5], H. -Wu[5], S.-Y. Shen[4], J.-R. Shi[5],
B.-L. He[5], Y.-J. Lei[5], Y.-B. Li[5], A.-L. Luo[5], Y.-H. Zhao[5], and H.-T. Zhang[5]

[1] Department of Astronomy, School of Physics, Peking University, Beijing 100871, China; aiyl@pku.edu.cn
[2] School of Physics and Astronomy, Sun Yat-Sen University, Guangzhou 510275, China
[3] Kavli Institute for Astronomy and Astrophysics, Peking University, Beijing 100871, China
[4] Shanghai Astronomical Observatory, Chinese Academy of Sciences, Shanghai 200030, China
[5] Key Laboratory of Optical Astronomy, National Astronomical Observatories, Chinese Academy of Sciences 100012, Beijing, China
[6] Yunnan Observatories, Chinese Academy of Sciences, Kunming 650011, China
[7] Key Laboratory for the Structure and Evolution of Celestial Objects, Chinese Academy of Sciences, Kunming 650011, China

ABSTRACT

We present preliminary results of the quasar survey in the Large Sky Area Multi-Object Fiber Spectroscopic Telescope (LAMOST) first data release (DR1), which includes the pilot survey and the first year of the regular survey. There are 3921 quasars reliably identified, among which 1180 are new quasars discovered in the survey. These quasars are at low to median redshifts, with a highest z of 4.83. We compile emission line measurements around the Hα, Hβ, Mg II, and C IV regions for the new quasars. The continuum luminosities are inferred from SDSS photometric data with model fitting, as the spectra in DR1 are non-flux-calibrated. We also compile the virial black hole mass estimates, with flags indicating the selection methods, and broad absorption line quasars. The catalog and spectra for these quasars are also available. Of the 3921 quasars, 28% are independently selected with optical–infrared colors, indicating that the method is quite promising for the completeness of the quasar survey. LAMOST DR1 and the ongoing quasar survey will provide valuable data for studies of quasars.

Key words: catalogs – quasars: general – surveys

Supporting material: FITS file, machine-readable and VO table

1. INTRODUCTION

A huge effort has been undertaken to find quasars since the first one was discovered in 1963 (Schmidt 1963). The most distant quasar, $z = 7.085$, was identified by the United Kingdom Infrared Telescope (UKIRT) Infrared Deep Sky Survey (UKIDSS; Mortlock et al. 2011). Quasars, with accretion onto their central supermassive black holes, emit a broad range of electromagnetic waves, from radio to γ-ray (Antonucci 1993). They can be one hundred times brighter than their host galaxies. Quasars are important extragalactic objects in astrophysics that are used to map black hole growth (e.g., Kollmeier et al. 2006) and to probe the galaxy evolution and intergalactic medium (e.g., Hennawi & Prochaska 2007; Ross et al. 2009).

Quasars can be selected from stellar and normal galaxies in different wavelength ranges, from radio to γ-ray, based on their distinguished spectral energy distribution, huge luminosity, and variations. The highest yields of quasars are from the Sloan Digital Sky Survey (SDSS; e.g., Shen et al. 2011; Pâris et al. 2012). The Two-Degree Fields survey (2dF) has also identified a large sample of quasars (Boyle et al. 2000). Both SDSS and 2dF select quasar candidates mainly based on multi-color ultraviolet (UV)/optical photometric data, i.e., UV excess (Fan et al. 2000; Richards et al. 2002, 2004, 2009; Smith et al. 2005). The completeness and efficiency of this selection are higher at redshifts less than 2, but drop significantly at $2.2 \leqslant z \leqslant 3.5$, the range in which the peak of the quasar luminosity function is reached (Fan 1999; Richards et al. 2002, 2006; Schneider et al. 2007). The efficiency can be improved by combining the quasar selections based on the variability

(Graham et al. 2014; MacLeod et al. 2011; Wu et al. 2011; Palanque-Delabrouille et al. 2011; Morganson et al. 2014), for which multi-epoch data are required.

The infrared survey is promising in its potential for finding quasars at high redshifts and improving the completeness and efficiency of quasar surveys at low and median redshifts. More quasars are identified with the UKIDSS survey (e.g., Warren et al. 2000; Croom et al. 2001; Sharp et al. 2002; Hewett et al. 2006; Chiu et al. 2007; Maddox et al. 2008, 2012; Smail et al. 2008), and other studies are explored to select quasar candidates with SDSS/UKIDSS colors (e.g., Wu & Jia 2010). Compared to the limited survey area of UKIDSS, the all sky survey *Wide-field Infrared Survey Explorer* (*WISE*; Wright et al. 2010; Cutri et al. 2012) data release shines more light on quasar surveys. Wu et al. (2012) proposed criteria for quasar candidate selections with SDSS/*WISE* colors. With this method they detected an ultra-luminous quasar at a redshift of 6.3 (Wu et al. 2015).

Recently, data-mining algorithms have been applied to the search for quasar candidates. These methods have been exploited in the SDSS-III Baryon Oscillation Spectroscopic Survey (BOSS; Ross et al. 2012), including an extreme deconvolution method (XDQSO; Bovy et al. 2011), a kernel density estimator (KDE; Richards et al. 2004, 2009), a likelihood method (Kirkpatrick et al. 2011), and a neutral network method (Yéche et al. 2010). Peng et al. (2012) also developed a classification system based on a support vector machine (SVM). Generally, different selection methods are combined to reach a higher completeness in quasar sky surveys.

The Large Sky Area Multi-Object Fiber Spectroscopic Telescope (LAMOST) is the Chinese multi-fiber telescope. Some quasar candidates, selected by optical–infrared colors, have been identified during the commission survey phase (Wu et al. 2010). The LAMOST regular survey began in 2012, and there were ~70,000 quasar candidates observed before 2013 June, as released in the LAMOST first data release. These objects are selected with several quasar selection methods. In this paper we describe the LAMOST quasar survey and candidate selections in Section 2. Spectral measurements and black hole mass estimations for the new quasars are described in Sections 3 and 4, respectively. Section 5 presents the description of the quasar catalog. Section 6 is the discussion. We use a Λ-dominated cosmology with $h = 0.7$, $\Omega_m = 0.3$, and $\Omega_\Lambda = 0.7$ throughout the paper.

2. SURVEY OUTLINE

LAMOST is a reflecting Schmidt telescope with an effective aperture of 4 m. It is equipped with 4000 fibers that can be deployed across a $5°$ (diameter) field of view. The spectral resolution is $R \sim 1800$ over the wavelength range from 3800 to 9100 Å, which is divided into red and blue spectroscopic channels. Two arms of each spectrograph cover this wavelength range with an overlap of 200 Å. The blue spectral coverage is 3700 Å ~ 5900 Å, and the red is 5700 Å ~ 9000 Å (Cui et al. 2012; Zhao et al. 2012). The raw data were reduced with LAMOST two-dimensional pipelines, including bias subtraction, cosmic-ray removal, spectral tracing and extraction, wavelength calibration, flat fielding, and sky subtraction (Luo et al. 2012).

LAMOST began a pilot survey in 2011 October and a regular survey in 2012 September. The regular survey, carried out over five to six years, has two major components: the LAMOST Experiment for Galactic Understanding and Exploration (LEGUE) and the LAMOST Extragalactic Survey (LEGAS; Zhao et al. 2012). LEGAS only uses a small part of the available observing time due to the limitations of the LAMOST site, especially the bright sky background and poor seeing. The first data release (DR1) contains spectra taken before 2013 June (Luo et al. 2015). In this paper we present the results of the quasar survey from LEGAS, while the quasars discovered in the vicinity of the Andromeda and Triangulum galaxies in LEGUE are presented in Huo et al. (2013).

2.1. Target Selections

The main objective of the LEGAS quasar survey is to discover more new quasars. Most candidates are selected based on SDSS photometry, of which the objects are required to be point sources in SDSS DR9 (Ahn et al. 2012) and brighter than $i = 20$. The SDSS point-spread function (PSF) magnitudes are used with the Galactic extinction corrected (Schlegel et al. 1998). A bright magnitude limit, $i = 16.0$, is required to avoid saturation and cross-talk in the spectra. The primary targets are selected based on the following.

1. *Optical–infrared colors*. The investigations of quasar selection based on SDSS-UKIDSS/*WISE* colors are described in Wu & Jia (2010) and Wu et al. (2012). These quasar candidates are selected based on their locations in multi-dimensional SDSS optical and UKIDSS/*WISE* infrared color space. In the LAMOST quasar survey, those selected SDSS point sources are

matched with UKIDSS/Large Area Survey (LAS) DR8[8] and the *WISE* All-Sky Data Release within a positional offset of $3''$ and $6''$, respectively. Only sources flagged as unaffected by known artifacts in all of the four bands are considered in the *WISE* catalog. The SDSS magnitudes referred to in the following are in AB magnitudes and the UKIDSS/*WISE* magnitudes are in Vega magnitudes. For the SDSS-UKIDSS matched objects we select quasar candidates with the criteria of $Y - K > 0.46(g - z) + 0.82$ or $J - K > 0.45(i - Y - 0.366) + 0.64$ (Wu & Jia 2010). For the SDSS-*WISE* matched objects the quasar candidate selection criteria in the regular survey are $w1 - w2 > 0.57$ or $z - w1 > 0.66(g - z) + 2.01$ (Wu et al. 2012). These selections mostly select quasars with redshift less than 4.

2. *Data-mining algorithms*. A combination of quasar selections with data-mining methods: SVM classifiers (SVM; Peng et al. 2012), extreme deconvolution method (XDQSO; Bovy et al. 2011), and a KDE (Richards et al. 2009).

The primary sample described above was supplemented by the objects selected via multi-wavelength (optical-X-ray/radio) data matching, i.e., objects which have SDSS photometry in the X-ray sources of *XMM-Newton*, *Chandra*, and *ROSAT* and radio sources in FIRST (Becker et al. 1995) and NVSS (Condon et al. 1998). Among the above selected candidates there are known quasars in SDSS, and we include some of these known quasars in the LAMOST quasar survey. With the SDSS spectra of these known quasars we can test the calibrations of LAMOST spectroscopy and investigate the spectroscopic variability of quasars. Finally, the LAMOST quasar survey also includes a small number of quasars selected using serendipitous methods.

2.2. Spectroscopy

LAMOST LEGAS spectroscopic observations are taken in a series of at least three 30 minute exposures. There are 70,290 quasar candidates observed, with 82,625 spectra in DR1. Among them, there are ~10,000 objects identified as QSO, STAR, or GALAXY by the LAMOST pipeline, while the remaining majority, ~60,000, are classified as UNKNOWN. For some of these UNKNOWN, the spectra are taken under non-photometric conditions, i.e., varying seeing and/or cloudy. Unstable efficiency for some fibers also contributes to the high fraction of UNKNOWN. The other factor is that the magnitude cutoff at $i = 20$ for quasar candidate selection is too faint for the LAMOST LEGAS survey. In Figure 1 we present the SDSS i-band PSF magnitude distributions of the observed quasar candidates. It is clear that the mean magnitude of these UNKNOWN, $i = 19.09$, is around one magnitude fainter than that of the identified QSO/STAR. The median signal-to-noise ratio (S/N) per pixel in the wavelength regions of 4000–5700 and 6200–9000 Å of LAMOST spectra are also shown in the figure. Most of these UNKNOWN have spectra with relatively lower S/N compared to QSO/STAR.

---

[8] The UKIDSS project is defined in Lawrence et al. (2007). UKIDSS uses the UKIRT Wide Field Camera (Casali et al. 2007) and a photometric system described in Hewett et al. (2006). The pipeline processing and science archive are described in Hambly et al. (2008).
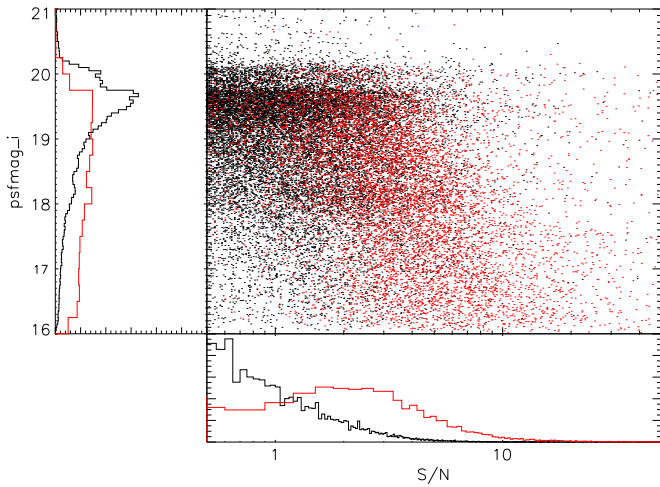
Figure 1. Distributions of the S/N of LAMOST spectra and SDSS i-band PSF magnitudes for the objects classified as UNKNOWN (black) and QSO/STAR (red) from the pipeline in the LAMOST LEGAS survey.

Figure 2. Redshift distributions of the reliably identified 3921 quasars in LAMOST DR1.

For the ~10,000 identified QSO/STAR we visually inspect the spectra to confirm the identifications with the Java program ASERA (Yuan et al. 2013). The misclassified objects are rejected or re-classified according to the S/N. For quasars we only keep the spectra with at least one high S/N emission line to ensure the reliability of systematic redshift estimations. The visually inspected redshift is set by eye at the maximum of the available typical quasar emission lines, i.e., [O III], Mg II, C III, and C IV. If the redshift provided by the pipeline does not match the one estimated in ASERA, we manually correct the redshift given by the pipeline, when the spectrum has at least two emission lines available.

Finally, there are 3921 quasars and 5355 stars with reliable identifications as secured in ASERA. The highest redshift of the identified quasar is 4.83 and most of the quasars are at low to median redshift with redshifts less than 3, as shown in Figure 2. The drop in the redshift distribution at $z \sim 1.0$ is from inefficient identifications in this redshift range as the emission line of Mg II moves into the overlaps of the blue and red channels.

Among the visually secured LAMOST quasars there are 2741 previously known quasars as matched with NED/SDSS DR10. For 95% of them the redshift differences between SDSS and LAMOST are less than 0.1. For the objects with redshift differences larger than 0.2 we visually checked the SDSS and LAMOST spectra. The differences come from incorrect estimations of redshifts in LAMOST due to low S/N of the spectra or misidentifications of the emission lines. Time lags between LAMOST and SDSS spectroscopic observations range from months to decades, which are suitable to study quasar variability on both short and long timescales. In the DR1 LAMOST release the spectra were non-flux-calibrated. Thus it is much more applicable to study line profile variabilities of quasars, instead of flux variations. In Figure 3 we present LAMOST and SDSS spectra as examples of quasars with consistent redshifts, including the one with the highest redshift ($z = 4.83$) identified by LAMOST.

The main purpose of this paper is to compile a catalog for the 1180 new quasars discovered in LAMOST DR1. The redshifts and i-band absolute magnitudes for these quasars are shown in Figure 4. Here luminosity is indicated using the (continuum and emission line) K-corrected, i-band absolute magnitude,
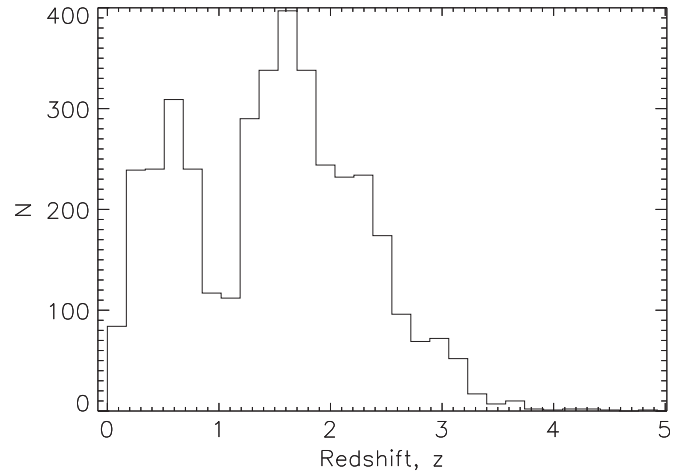
$M_i(z = 2)$, normalized at $z = 2$ (Richards et al. 2006). In the following we present detailed descriptions about the emission line measurements and black hole mass estimations for these quasars.

3. SPECTRAL MEASUREMENTS

We measure the properties of the Hα, Hβ, Mg II, and C IV lines with spectral fittings. These lines are the typical strong emission lines of quasars and are calibrated as virial black hole mass estimators. The fits are based on the MPFIT package (Markwardt 2009), which performs χ^2 minimization using the Levenberg–Marquardt technique. Details of the spectral fitting in the optical and near-ultraviolet regions have been described in the literature (e.g., Dong et al. 2008; Wang et al. 2009a; Ho et al. 2012). The crossover between the red and blue channels, the wavelength range of 5700–6200 Å in observed frame, is masked out. All the LAMOST spectra are corrected for Galactic extinction using the extinction map of Schlegel et al. (1998) and the reddening curve of Fitzpatrick (1999). The spectra are shifted back to their rest frames in the fitting.

For each line we first fit a local pseudo-continuum, i.e., a simple power law or a power law plus an Fe II multiplet emission, to the wavelength regions least contaminated by the broad line emission. The pseudo-continuum fitting windows for each line are referred to those used in Shen et al. (2011). The parameters of normalization α and slope β of the power-law continuum are set as free. The parameters of the Fe II multiplet emissions, i.e., normalization, velocity shift relative to the systemic redshift, and broadening velocity, are also set as free. The fitted pseudo-continuum emission is subtracted from the spectra and the leftover emission-line spectra are fitted with Gaussian and/or Gaussian–Hermite profiles. Below we describe the detailed fitting procedures for each line.

3.1. Hα and Hβ

We fit the spectra of quasars with $z \lesssim 0.30$ for Hα and $z \lesssim 0.75$ for Hβ. The fitting windows of the power law plus Fe II emission are [6000, 6250] Å and [6800, 7000] Å for Hα and [4435, 4700] Å and [5100, 5535] Å for Hβ. The template of optical Fe II emission is from Véron-Cetty et al. (2004). A Gaussian function is used to model the emission lines. Both Hα and Hβ emission lines are modeled with one narrow and one
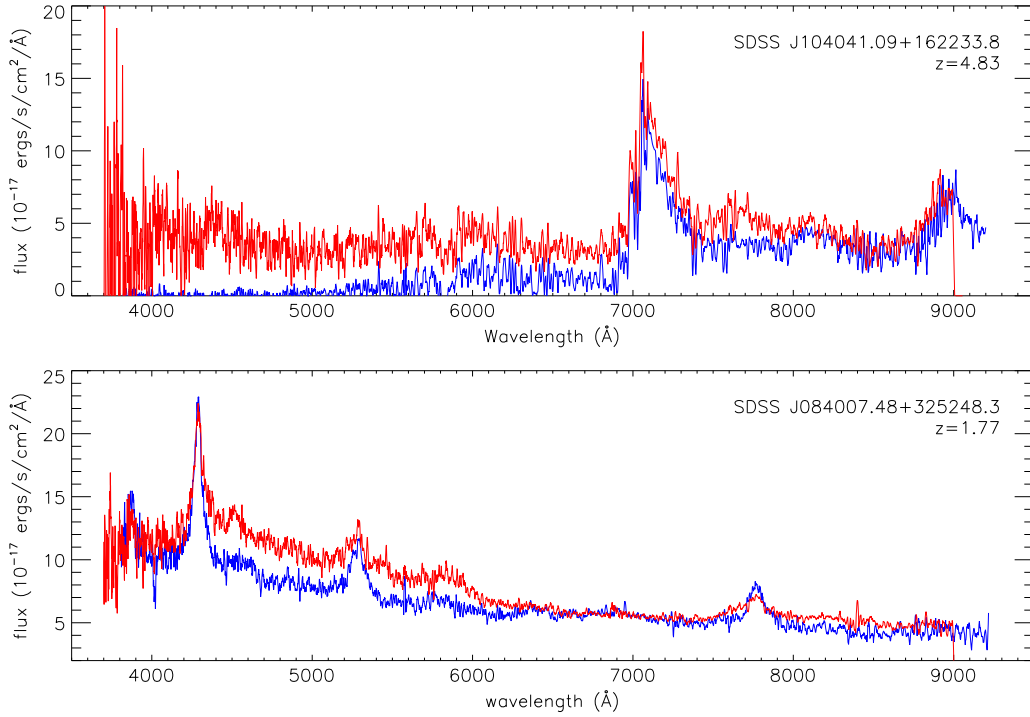
Figure 3. Examples of the quasars with spectroscopic observations in LAMOST (blue) and SDSS (red). The non-calibrated LAMOST spectra are scaled to those of SDSS, and all the spectra are smoothed with a boxcar of 5 pixels for illustration.
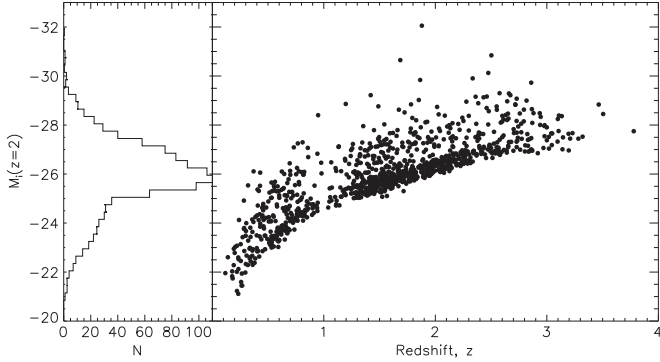

Figure 4. Distributions of the new quasars discovered in LAMOST DR1 in luminosity–redshift space, where the left panel shows the luminosity histograms.

broad component. The broad component is fitted with as many Gaussians as statistically justified (see Dong et al. 2008 for details). All of the narrow emission lines except the [O III] doublet are fitted with a single Gaussian. The upper limits of the FWHM for the narrow lines are set to be 1200 km s^{-1}.

Each line of the [O III] $\lambda\lambda4959$, 5007 doublet is modeled with two Gaussians, one accounting for the line core and the other for a possible blue wing as seen in many objects (e.g., Greene & Ho 2005a, Komossa et al. 2008, Wang et al. 2009b). The doublet is assumed to have the same redshifts and profiles, with the flux ratio fixed to the theoretical value of 3. Velocity offsets and line widths of the doublet core component are tied to those of the narrow Hβ component. The velocity offsets and line widths of [N II] $\lambda\lambda6548$, 6584 and [S II] $\lambda\lambda6717$, 6731 are tied to those of the Hα narrow component. The relative flux ratio of the two [N II] components is fixed to 2.96. We present the fittings to Hβ and Hα lines in Figure 5 as illustrations.

3.2. Mg II and C IV

We fit the spectra of quasars with $0.40 \lesssim z \lesssim 1.76$ for the Mg II line, and $z \gtrsim 1.58$ for C IV. The pseudo-continuum fitting windows are [2200, 2700] Å and [2900, 3090] Å for Mg II and [1445, 1465] Å and [1700, 1705] Å for C IV. The ultraviolet Fe II template from Tsuzuki et al. (2006) is included in the continuum modeling of Mg II, but not for C IV. This is mainly because Fe II emission is usually not strong for C IV, and inclusion of Fe II emission will add uncertainties to the fitted parameters based on the data quality of LAMOST.

Each of the Mg II $\lambda\lambda2796$, 2803 doublet components are modeled with one narrow and one broad component. The narrow component is modeled with a single Gaussian, and the upper limit of FWHM is set to be 900 km s^{-1} (Wang et al. 2009a). We model the broad component with a truncated five-parameter Gauss-Hermite series (van der Marel & Franx 1993; see also Salviander et al. 2007). The broad components of the Mg II doublet lines are set to have the same profile, with flux ratio set to be between 2:1 and 1:1 (Laor et al. 1997). The same prescription is applied to the narrow components. For C IV we model the line with one Gaussian and one Gaussian–Hermite function to obtain a smooth realization of the line profile. We do not set an upper limit for the FWHM of the Gaussian function since there are still debates on whether a strong narrow component exists for the C IV line (Baskin & Laor 2005). We present the fittings to Mg II and C IV lines in Figure 6 as illustrations.

The fittings to Mg II and C IV emission lines are frequently affected by narrow or broad absorption features. The effects on the fittings from the broad absorption trough are hard to reduce in the automatic fitting procedure, while the impact of narrow or moderate absorption features can be alleviated (Shen et al. 2011). We mask out 3σ outliers below the 20 pixel boxcar-smoothed spectrum to reduce the effects of narrow or
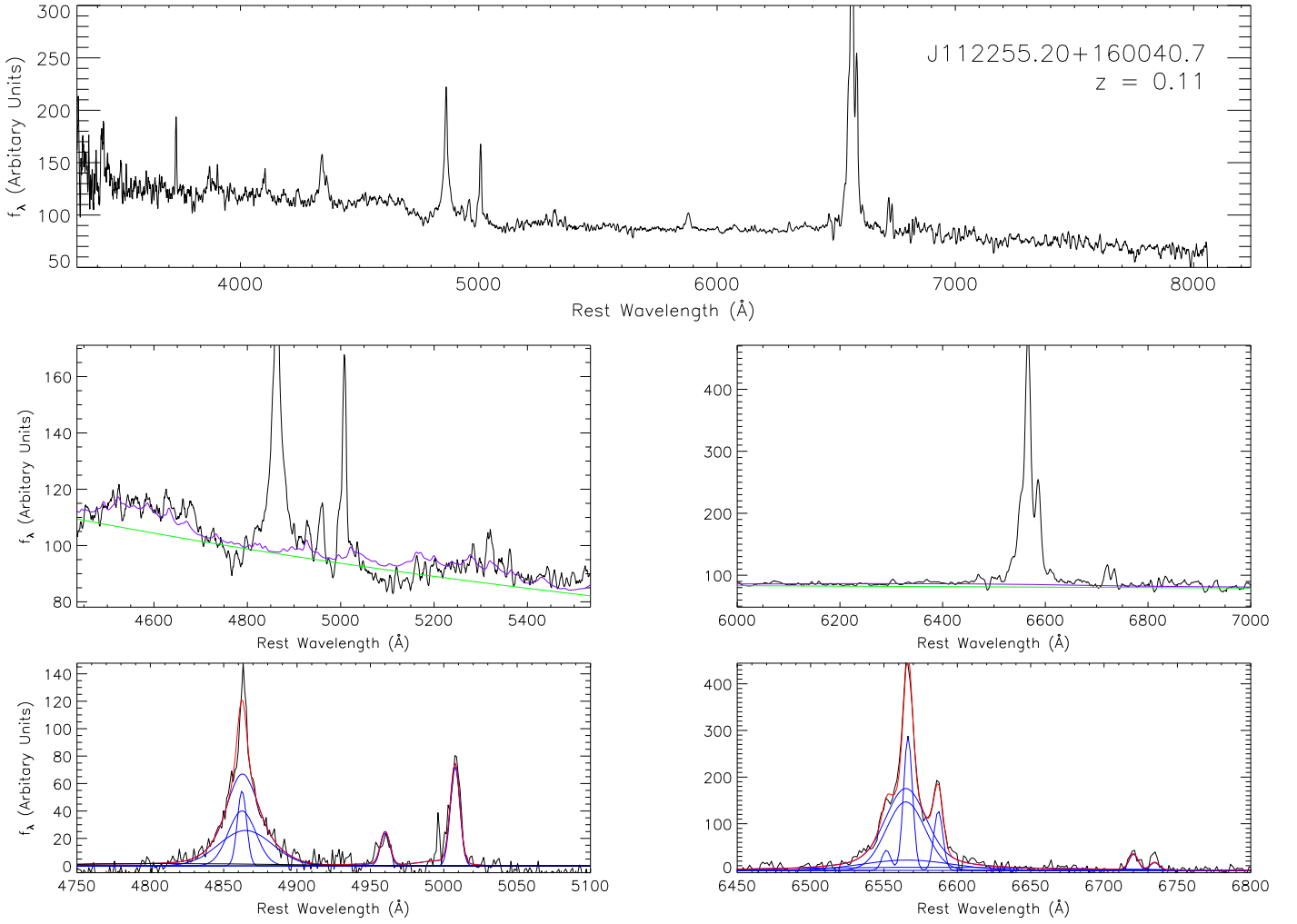
Figure 5. Representative example of the fitting applied to the Hβ + [O III] and Hα + [N II] ranges. The upper panel is the observed spectrum; middle panels show the pseudo-continuum fitting with power-law (green) and Fe II multiplets (cyan lines indicate the Fe II plus power-law emission); bottom panels are the results of deblending procedures applied to Hβ + [O III] and Hα + [N II] emission lines, in which the combination of models (red) and individual components (blue) are shown. The observed spectra are smoothed with a boxcar of 5 pixels for the illustration.

moderate absorptions on the C IV and Mg II emission line fittings.

3.3. Reliability of Spectral Fittings

We visually inspect the fitting results for each object. Most of the fits to the spectrum with high S/N are acceptable, as shown in Figures 5 and 6. The bad fits include spectra with low S/N, too few good pixels in the fitting region, or objects with peculiar continuum and emission line properties, such as broad absorption line quasars and disk emitters. A flag is given for each line based on visual inspections to indicate the quality of the spectral fitting. Flag = 0 means that the fitting is acceptable and the inferred parameters are mostly reliable, while flag = −1 means that the line measurements may be spurious.

4. CONTINUUM LUMINOSITY AND VIRIAL BLACK HOLE MASS

We fit the five-band SDSS photometry with model spectra to estimate the continuum luminosity for the new quasars. In the first step we extract SDSS PSF magnitudes for only the quasars

that have clean photometry[9] in the SDSS database. The Galactic extinction corrected SDSS *ugriz* magnitudes are converted to the corresponding magnitudes on the AB system.[10] These AB magnitudes are then turned into the flux density, F_λ, at the effective wavelength of each filter. We then fit the five data points, F_λ, of each quasar at rest frame with model spectra composed of two components: continuum emission and line emission. The features of these two components are referred to those of the composite quasar spectra in Vanden Berk et al. (2001, hereafter VB01). As described in VB01 the continuum of composite quasar spectra is well fitted by broken power laws, and the features left after the subtraction of the continuum in the median composite quasar spectra are taken as the template of line emission in our model.

In our fitting, the indices of the broken power law and normalization of line emission are set as free parameters. The break of the two power laws is set to the value of 4661 Å, which is similar to the value inferred from median composite spectra in VB01. The normalization of the continuum is tied to the mean value of the total emission in the regions of
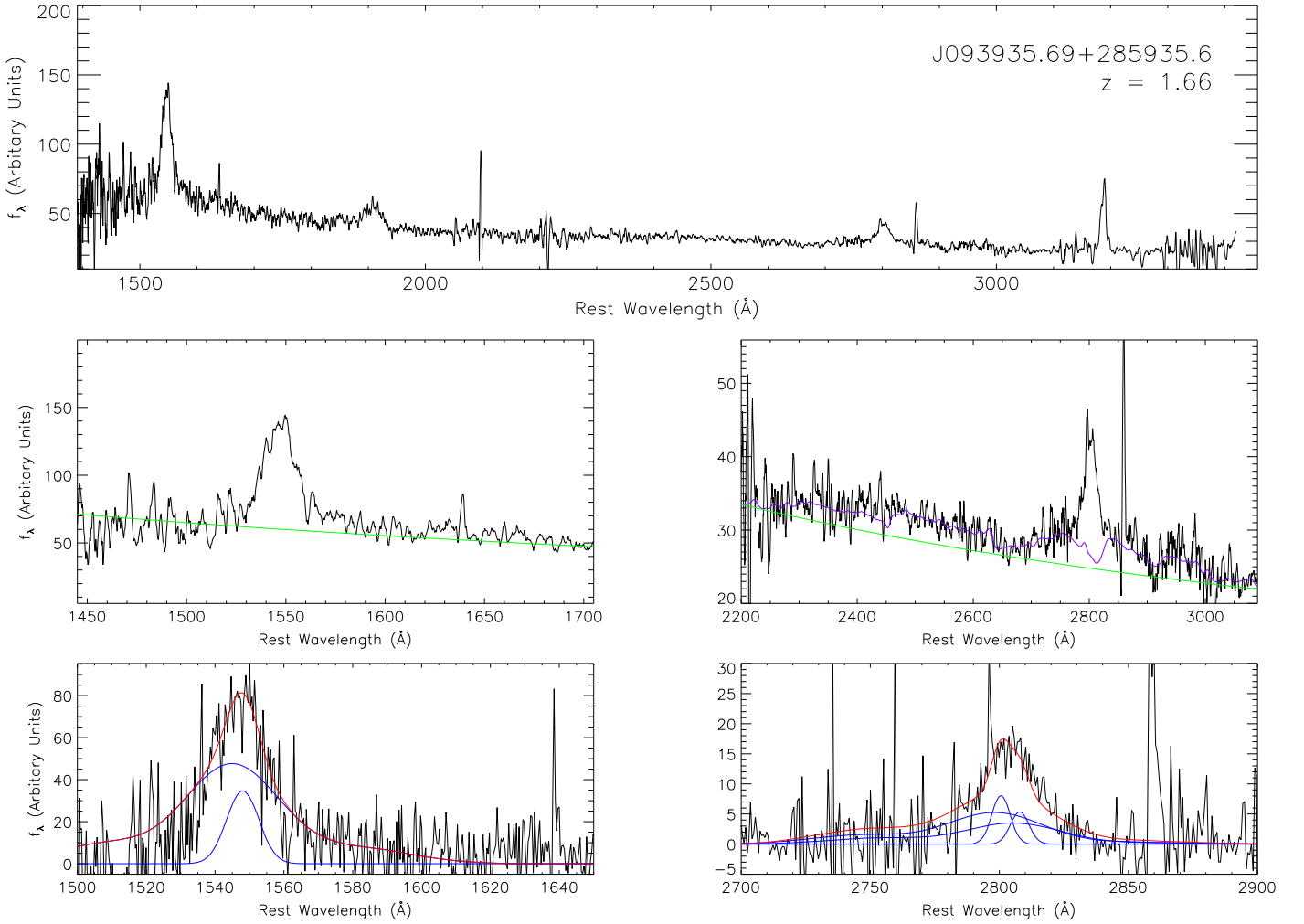

Figure 6. Representative example of the fitting applied to Mg II and C IV lines. The upper panel is the observed spectrum; middle panels show the pseudo-continuum fitting with power-law (green) and Fe II multiplets (cyan lines indicate the Fe II plus power-law emission); bottom panels are the results of deblending procedures applied to Mg II and C IV emission lines, in which a combination of models (red) and individual components (blue) are shown. The observed spectra are smoothed with a boxcar of 5 pixels for the illustration.

1350–1365 and 4200–4230 Å. The values of these two regions are taken from VB01, in which they fit the continuum. Blueward of Lyα we only scale the composite median quasar spectra. The fitting is performed by minimizing the chi-squared, χ^2.

We present examples of the modeling in Figure 7. As shown in the figure, the continuum model of quasars with $z \gtrsim 1$ is actually a single power law since for these quasars the value of the break of the two power laws, set in our model, moves out of the LAMOST wavelength region. For these quasars the degrees of freedom (dof) is 2, which is one more than that of the quasars with $z < 1$. The mean frequency power-law index inferred from the fitting, $\langle \alpha_\nu \rangle$, is −0.43 from ∼1300 to 4661 Å and –1.60 redward of ∼4661 Å, which are in good agreement with the values found in composite quasar spectra in VB01.

The distribution of the reduced chi-squared, χ^2_ν, is shown in Figure 8. In the figure we mark the values of the reduced chi-squared, $\chi^2_{\nu,0.05}$, that correspond to a probability of 0.05 of obtaining a value $\chi^2_\nu > \chi^2_{\nu,0.05}$. The $\chi^2_{\nu,0.05}$ is 3.841 with dof of 1 and 2.996 with dof of 2. The fittings with $\chi^2_\nu < \chi^2_{\nu,0.05}$ are good fits in the statistical significance level. However, not all of the fits with relatively larger χ^2_ν are unacceptable based on

visual inspections. In Figure 8 we also present the distribution of the fraction of continuum emission accumulated in the data fitting wavelength range (from only a rest-frame wavelength of 1200 Å if the data extend blueward of Lyα). The fractions of continuum emission are mostly in a range greater than 60%, dispersed around the values (84%–88%) of those in VB01. The fractions with extremely high values are mostly derived from the quasars with bad fitting. In a loose constraint we reject the fittings with fraction values greater than 0.989.

With the inferred continuum luminosity, i.e., L_{5100}, L_{1350}, and L_{3000}, and corresponding broad line width we can estimate the virial black hole masses with

$$\log\left(\frac{M_{\mathrm{BH}}}{M_\odot}\right) = \alpha + \beta \log\left(\frac{\lambda L_\lambda}{10^{44}\ \mathrm{erg\ s}^{-1}}\right)$$
$$+ \gamma \log\left(\frac{\mathrm{FWHM}}{\mathrm{km\ s}^{-1}}\right). \quad (1)$$

The coefficients α, β, and γ are empirically calibrated and the values differ in the calibrations with different measurements of emission lines and samples (e.g., McLure & Dunlop 2004; Greene & Ho 2005b; Vestergaard & Peterson 2006; Wang
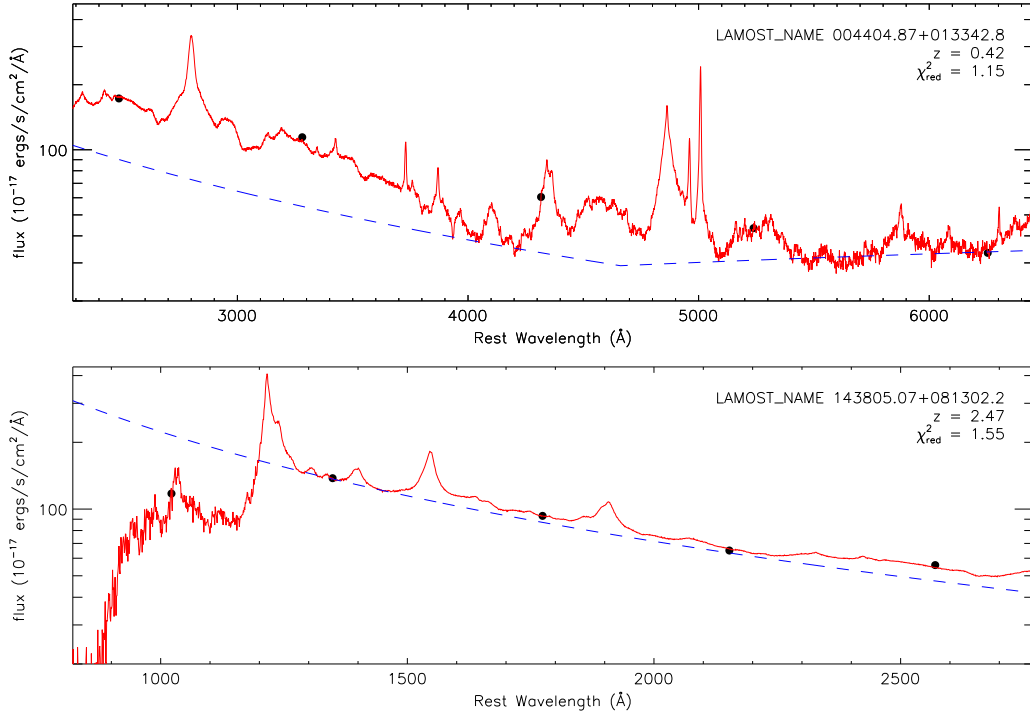
Figure 7. Examples of the estimation of the continuum luminosity with model fitting to SDSS photometry (black points). The fitted total model spectra (red lines) and power law continuum (blue dashed lines) are shown.
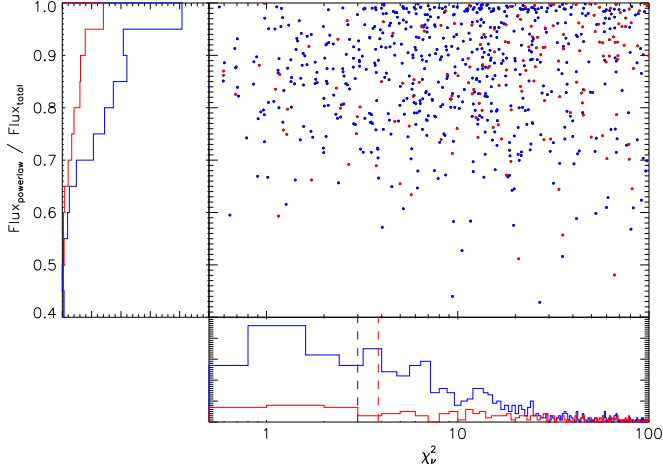

Figure 8. Distribution of reduced chi-squared, χ_ν^2, and flux ratio of the continuum to total emission in the data fitting range. Red points are the quasars with $z < 1$, and blue points are the rest. The vertical dashed lines label the values of 3.841 and 2.996 of $\chi_{\nu,0.05}^2$, which correspond to a probability of 0.05 of obtaining a value $\chi_\nu^2 > \chi_{\nu,0.05}^2$ with dof of 1 and 2.

Figure 9. Filled circles are the new quasars discovered in LAMOST DR1 with estimated black hole masses based on emission lines of $H\beta$ (black), Mg II (green), and C IV (blue). Small gray dots are SDSS quasars from Shen et al. (2011).

et al. 2009a; Zuo et al. 2015). In this paper for $H\beta$-based and C IV-based estimates we use the virial black hole mass calibrations from Vestergaard & Peterson (2006), and for Mg II-based from Wang et al. (2009a). The FWHM of broad Mg II $\lambda2796$ and the FWHM of the whole C IV emission are used in the estimations following the FWHM definitions adopted in these calibrations. The black hole masses are estimated only for those quasars with both inferred continuum luminosity and broad line widths flagged as reliable.

We note that the continuum luminosity estimations described above introduce additional uncertainties to the black hole mass estimations compared to those from single-epoch spectra. The uncertainties come from model fitting to the SDSS photometric data and intrinsic variations of quasar luminosity. Time lags between SDSS photometric data and LAMOST spectra are ~10 years. On this timescale the optical/ultraviolet emissions of quasars are variable with amplitudes of 0.1–0.2 mag (e.g., Vanden Berk et al. 2004; Zuo et al. 2012; Ai et al. 2013). To justify our estimations we present the apparent trend of the black hole masses with redshifts in Figure 9. It is evident that the distributions of the black hole masses for these LAMOST quasars are overlapped with those of SDSS DR7 quasars from Shen et al. (2011). The result supports that our continuum modeling is mostly valid and the estimated black hole masses can be taken as a proxy for these new quasars.

Table 1
Catalog Format for the 1180 New Quasars Discovered in LAMOST DR1

Column	Name	Format	Description
1	LAMOST_NAME	STRING	LAMOST DR1 designation hhmmss.ss+ddmmss (J2000)
2	R.A.	DOUBLE	R.A. in decimal degrees (J2000)
3	Decl.	DOUBLE	Decl. in decimal degrees (J2000)
4	MJD	LONG	MJD of spectroscopic observation
5	PLANID	STRING	Spectroscopic plan identification
6	SPID	STRING	Spectrograph identification
7	FIBERID	LONG	Spectroscopic fiber number
8	Z_VI	DOUBLE	Redshift from visual inspection
9	ZWARNING	LONG	ZWARNING flag from visual inspection
10	MI_Z2	DOUBLE	M_i ($z = 2$), K-corrected to $z = 2$ following Richards et al. (2006)
11	NSPECOBS	LONG	Number of spectroscopic observations
12	SNR_SPEC	DOUBLE	Median S/N per pixel of the spectrum
13	FWHM_BROAD_HA	DOUBLE	FWHM of broad Hα in km s^{-1}
14	EW_BROAD_HA	DOUBLE	Rest frame equivalent width of broad Hα in Å
15	FWHM_NARROW_HA	DOUBLE	FWHM of narrow Hα in km s^{-1}
16	EW_NARROW_HA	DOUBLE	Rest frame equivalent width of narrow Hα in Å
17	EW_NII_6585	DOUBLE	Rest frame equivalent width of [N II]6584 in Å
18	EW_SII_6718	DOUBLE	Rest frame equivalent width of [S II]6717 in Å
19	EW_SII_6732	DOUBLE	Rest frame equivalent width of [S II]6731 in Å
20	EW_FE_HA	DOUBLE	Rest frame equivalent width of Fe within 6000–6500 Å in Å
21	LINE_NPIX_HA	LONG	Number of good pixels for the rest frame 6400–6765 Å
22	LINE_MED_SN_HA	DOUBLE	Median S/N per pixel for the rest frame 6400–6765 Å
23	LINE_FLAG_HA	LONG	Flag for the quality in Hα fitting
24	FWHM_BROAD_HB	DOUBLE	FWHM of broad Hβ in km s^{-1}
25	EW_BROAD_HB	DOUBLE	Rest frame equivalent width of broad Hβ in Å
26	FWHM_NARROW_HB	DOUBLE	FWHM of narrow Hβ in km s^{-1}
27	EW_NARROW_HB	DOUBLE	Rest frame equivalent width of narrow Hβ in Å
28	EW_OIII_4959	DOUBLE	Rest frame equivalent width of [O III]4959 in Å
29	EW_OIII_5007	DOUBLE	Rest frame equivalent width of [O III]5007 in Å
30	EW_FE_HB	DOUBLE	Rest frame equivalent width of Fe within 4435–4685A in Å
31	LINE_NPIX_HB	LONG	Number of good pixels for the rest frame 4750–4950 Å
32	LINE_MED_SN_HB	DOUBLE	Median S/N per pixel for the res tframe 4750–4950 Å
33	LINE_FLAG_HB	LONG	Flag for the quality in Hβ fitting
34	FWHM_MGII	DOUBLE	FWHM of the whole Mg II emission line in km s^{-1}
35	EW_MGII	DOUBLE	Rest frame equivalent width of the whole Mg II Å
36	FWHM_BROAD_MGII	DOUBLE	FWHM of the whole broad Mg II in km s^{-1}
37	EW_BROAD_MGII	DOUBLE	Rest frame equivalent width of the whole broad Mg II in Å
38	FWHM_BROAD_MGII_2796	DOUBLE	FWHM of the broad Mg II 2796 in km s^{-1}
39	FWHM_NARROW_MGII_2796	DOUBLE	FWHM of the narrow Mg II 2796 in km s^{-1}
40	EW_FE_MGII	DOUBLE	Rest frame equivalent width of Fe within 2200–3090 Å in Å
41	LINE_NPIX_MGII	LONG	Number of good pixels for the rest frame 2700–2900 Å
42	LINE_MED_SN_MGII	DOUBLE	Median S/N per pixel for the rest frame 2700–2900 Å
43	LINE_FLAG_MGII	LONG	Flag for the quality in Mg II fitting
44	FWHM_CIV	DOUBLE	FWHM of the whole C IV in km s^{-1}
45	EW_CIV	DOUBLE	Rest frame equivalent width of the whole C IV in Å
46	FWHM_BROAD_CIV	DOUBLE	FWHM of the broad C IV in km s^{-1}
47	EW_BROAD_CIV	DOUBLE	Rest frame equivalent width of the broad C IV in Å
48	FWHM_NARROW_CIV	DOUBLE	FWHM of the narrow C IV in km s^{-1}
49	EW_NARROW_CIV	DOUBLE	Rest frame equivalent width of the narrow C IV in Å
50	LINE_NPIX_CIV	LONG	Number of good pixels for the rest frame 1500–1600 Å
51	LINE_MED_SN_CIV	DOUBLE	Median S/N per pixel for the rest frame 1500–1600 Å
52	LINE_FLAG_CIV	LONG	Flag for the quality in C IV fitting
53	ALPHA_LAMBDA_1	DOUBLE	Wavelength power-law index from ~1300 to 4661 Å
54	ALPHA_LAMBDA_2	DOUBLE	Wavelength power-law index redward of 4661 Å
55	MODEL_PHOT_REDCHI2	DOUBLE	Reduced chi-square
56	LOGL5100	DOUBLE	Monochromatic luminosity at 5100 Å (erg s^{-1})
57	LOGL3000	DOUBLE	Monochromatic luminosity at 3000 Å (erg s^{-1})
58	LOGL1350	DOUBLE	Monochromatic luminosity at 1350 Å (erg s^{-1})
59	LOGBH_HB	DOUBLE	Virial BH mass based on Hβ ($M_\odot$)

Column	Name	Format	Description
60	LOGBH_MgII	DOUBLE	Virial BH mass based on Mg II ($M_\odot$)
61	LOGBH_CIV	DOUBLE	Virial BH mass based on C IV($M_\odot$)
62	FPEAK	DOUBLE	FIRST peak flux density at 20 cm in mJy
63	BAL_FLAG	STRING	Broad absorption trough flag
64	FLAG_DATA_MINING	STRING	Flag of quasar selections based on data mining
65	FLAG_OI_COLOR	STRING	Flag of quasar selections based on optical–infrared color
66	FLAG_OTHERS	STRING	Flag of quasar selections from radio, X-ray, serendipitous algorithms.

(This table is available in its entirety in FITS format.)

5. THE SPECTRAL CATALOG

We present a compiled catalog for the new quasars identified in LAMOST DR1. All measured quantities are tabulated in the online catalog as a binary FITS table file at the LAMOST public website. We cross-correlate our quasar catalog with objects in the FIRST radio survey (Becker et al. 1995) within a 2″0 radius and list the FIRST peak flux density. A summary of the information contained in each of the columns is described in Table 1. Below we describe the specifics of the cataloged quantities.

1. LAMOST object designation: LAMOST Jhhmmss.ss +ddmmss.s(J2000, truncated coordinates). The "LAMOST J" for each entry is dropped.
2. R.A. and decl. (in decimal degrees, J2000).
3. Information of spectroscopic observation: Modified Julian date (MJD), spectroscopic plan identification (planID), spectrograph identification (spID), and spectroscopic fiber number (fiberID). These four numbers are unique for each spectrum named in the format of $spec - MJD - planID\_spID - fiberID.$ fits. Only information on the spectrum with the highest S/N is given if more than one spectroscopic observation is available for the quasar.
4. Redshift.
5. ZWARNING flag based on visual inspections. 1 = not robust.
6. $M_i(z = 2)$: absolute i-band magnitude. K-corrected to $z = 2$ following Richards et al. (2006).
7. NSPECOBS: number of spectroscopic observations for the quasar.
8. SNR_SPEC: median S/N per pixel in the wavelength regions of 4000–5700 and 6200–9000 Å.
9. FWHM, rest-frame equivalent width (EW) for broad Hα, narrow Hα, [N II]6584, [S II]6717, and [S II]6731.
10. Rest-frame equivalent width of iron emission in 6000–6500 Å.
11. Number of good pixels and median S/N per pixel for the Hα region in 6400–6765 Å.
12. Flag indicates reliability of the emission line fitting results in the Hα region upon visual inspections. −1 = unacceptable; 0 = acceptable.
13. FWHM, rest-frame equivalent width for broad Hβ, narrow Hβ, [O III]4959, [O III]5007, fitted in the 4750–4950 Å region.
14. Rest-frame equivalent width of iron lines in 4435–4685 Å.
15. Number of good pixels and median S/N per pixel for the Hβ region in 4750–4950 Å.
16. Flag indicates reliability of the emission line fitting results in Hβ upon visual inspections. −1 = unacceptable; 0 = acceptable.
17. FWHM, rest-frame equivalent width for total Mg II emission line.
18. FWHM, rest-frame equivalent width for total broad Mg II lines.
19. FWHM for broad and narrow Mg II 2796 emission line.
20. Rest-frame equivalent width of iron lines in 2200–3090 Å.
21. Number of good pixels and median S/N per pixel for the Mg II region in 2700–2900 Å.
22. Flag indicates reliability of the emission line fitting results in Mg II upon visual inspections. −1 = unacceptable; 0 = acceptable.
23. FWHM, rest-frame equivalent width for total C IV emission line.
24. FWHM, rest-frame equivalent width for the Gaussian–Hermite component of the C IV line.
25. FWHM, rest-frame equivalent width for the Gaussian component of the C IV line.
26. Number of good pixels and median S/N per pixel for the C IV region in 1500–1600 Å.
27. Flag indicates reliability of the emission line fitting results in C IV upon visual inspections. −1 = unacceptable; 0 = acceptable.
28. Wavelength power-law index, α_λ, from ∼1300 to 4661 Å, and redward of 4661 Å.
29. Reduced chi-square in SDSS photometry modeling; –99 if not fitted.
30. Continuum luminosity at 5100, 3000, and 1350 Å.
31. Virial black hole masses with calibrations of Hβ (VP06), Mg II (Wang08), and C IV (VP06).
32. FIRST peak flux density at 20 cm.
33. Flag indicates whether a broad absorption trough is present in the spectra by visual inspection. 1 is set if visually identified as a broad absorption quasar.
34. Flag set as SVM, XD, or Richards09; mark quasars selected with corresponding data-mining method.
35. Flag set as W, or U; mark quasars selected with SDSS/UKIDSS or SDSS/*WISE* colors.
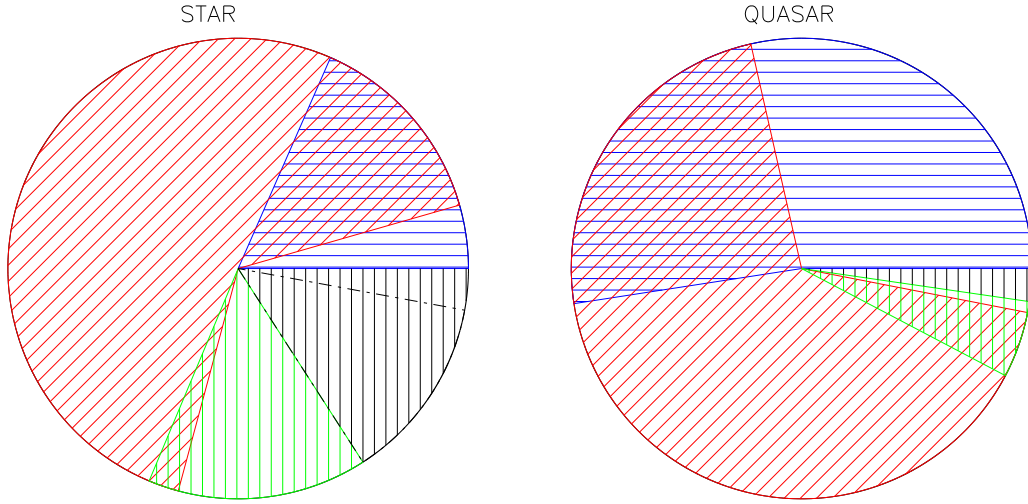36. Flag set as X-ray, RADIO, or S; mark quasars selected by X-ray, radio, or other serendipitous algorithms.

Figure 10. Illustration of the fractions of objects selected from optical–infrared colors (blue), data-mining algorithms (red), multi-wavelength (optical-X-ray/radio) matching (green), and serendipitous algorithms (black) for the 5355 stars and 3921 quasars in LAMOST DR1. The stars in the area of dash–dotted lines are observed in the pilot survey, of which the selections are a bit different from those in regular survey.
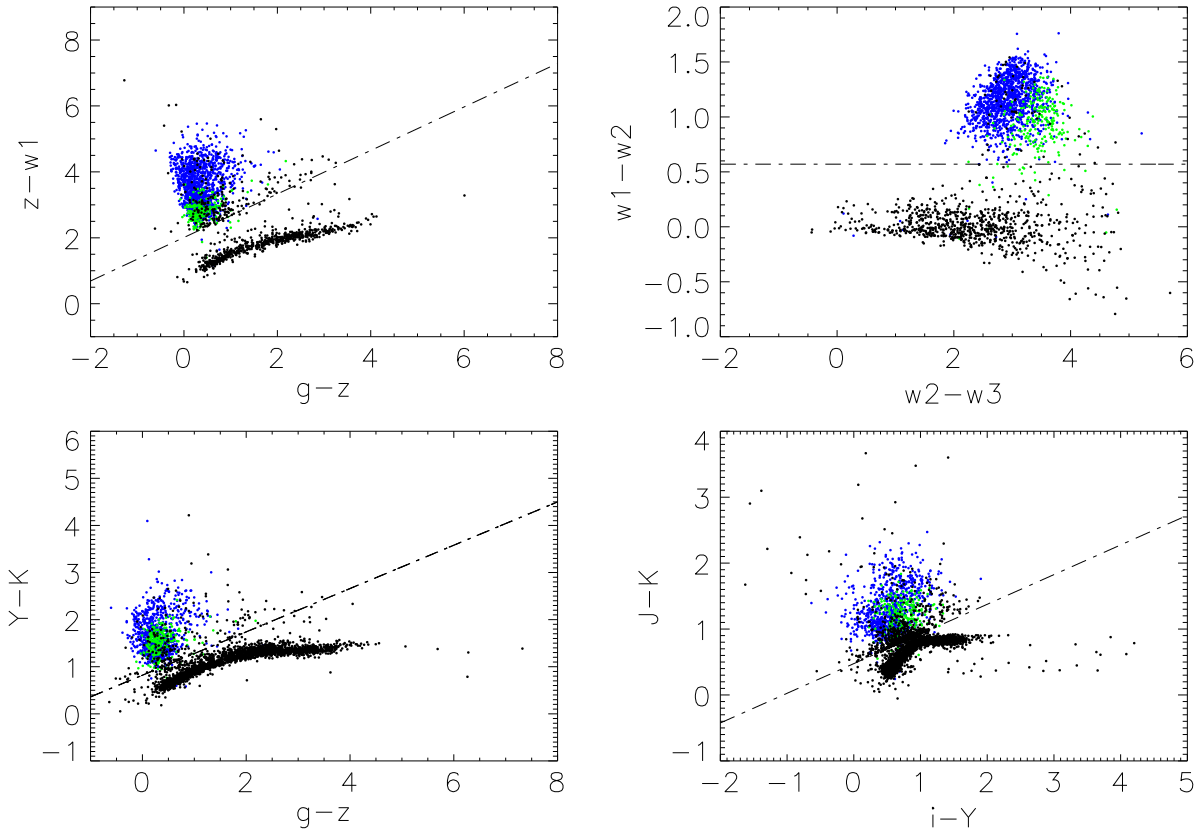

Figure 11. Distributions of 3921 quasars and 5355 stars (black dots) in SDSS-*WISE*/UKIDSS color diagram. Blue dots are the quasars with $z < 2.2$, and green are $z \gtrsim 2.2$. The dash–dotted lines indicate criteria used in the regular survey.

6. CONCLUSION AND DISCUSSION

We present our preliminary results of the LEGAS quasar survey in LAMOST DR1, which includes products from the pilot survey and the first year regular survey. We compile emission line measurements around the Hα, Hβ, Mg II, and C IV regions for the 1180 new quasars discovered in the survey. We also compile the virial black hole mass estimates, with flags indicating the selection methods, and broad absorption line

quasars. The catalog and spectra for these quasars are available online.

The candidates in the LEGAS quasar survey are selected from optical–infrared colors, data-mining algorithms, and multi-wavelength (optical–X-ray/radio) data matching. Object fractions selected from these methods for the reliably identified 5355 stars and 3921 quasars are shown in Figure 10. There are 28% of the quasars that were independently selected with optical–infrared colors, indicating that the method is quite

Table 2
Parameters of the 2741 Known Quasars

NAME	MJD	PLANID	SPID	FIBERID	FLAG_DATA_MINING	FLAG_OI_COLOR	FLAG_OTHERS
000009.38 + 135618.4	56214	EG000024N121601B01	11	084	/XD/Richards09	/W/U	⋯
000015.17 + 004833.3	56213	EG000023N024031B01	01	155	/XD/Richards09	/W/U	⋯
000116.00 + 141123.0	56214	EG000024N121601B01	11	228	/SVM/Richards09	/W/U	⋯
000234.51 + 051344.1	55893	F9302	14	194	⋯	/W/U	⋯
000338.63 + 114138.3	56214	EG000024N121601B01	08	011	/SVM/Richards09	/W/U	⋯
000520.22 + 052410.7	55893	F9302	03	110	⋯	/W/U	⋯
000725.53 + 133313.5	56214	EG000024N121601B01	12	152	/Richards09	/W/U	⋯
000727.05 + 024113.1	56213	EG000023N024031B01	13	092	/Richards09	/W/U	⋯
004342.54 + 372519.9	56221	M31012N38B1	10	203	⋯	/W	⋯
004448.32 + 372114.7	55862	M6201	10	216	⋯	/W	⋯
004547.23 + 041023.4	55892	F9202	16	193	⋯	/W/U	⋯
004610.29 + 010644.1	55892	F9202	02	143	⋯	/W	⋯
004613.78 + 004410.3	55892	F9202	02	216	/SVM	/W	/Xray
004818.98 + 394111.7	55863	M31_011N40_B1	08	102	⋯	/W	⋯
005008.49 + 011330.1	55892	F9202	01	163	/SVM	⋯	/Xray
005050.74 + 353642.9	55874	M31_012N38_B1	01	214	⋯	/W	

(This table is available in its entirety in machine-readable and Virtual Observatory (VO) forms.)

promising for completeness of low redshift quasars and searching for high redshift quasars (Wu et al. 2012, 2015; Yi et al. 2014; Wang et al. 2015). We have improved candidate selections in the regular survey compared to those in the pilot survey, in which a relatively larger fraction of stars is selected, as shown in the figure. We present the SDSS-*WISE*/UKIDSS color–color distributions of these quasars/stars in Figure 11, in which the criteria used in regular survey are shown in dash–dotted lines.

In DR1, a significantly high fraction (∼80%) of the observed candidates cannot be identified by the pipeline. Most of these UNKNOWN have spectra with low S/N due to non-photometric conditions, unstable fiber efficiency, and a fainter magnitude cutoff at $i = 20$ for quasar candidate selections. To increase the quasar identification efficiency we have adjusted the magnitude cutoff to $i = 19$ in the ongoing survey.

We provide the information from LAMOST spectroscopic observations and selection methods for the 2741 known quasars in Table 2. With LAMOST and SDSS spectra of these quasars, we can investigate quasar spectral variability on timescales from months to decades. It is worthwhile to launch follow-up studies for the interesting quasars discovered in DR1, such as those with broad absorption troughs in C IV and/or Mg II, double-peaked Balmer line profiles, etc. LAMOST DR1 and the ongoing survey will provide valuable data in the studies of quasars.

REFERENCES

Ahn, C. P., Alexandroff, R., Allende Prieto, C., et al. 2012, ApJS, 203, 21
Ai, Y. L., Yuan, W., Zhou, H., et al. 2013, AJ, 145, 90A
Antonucci, R. 1993, ARA&A, 31, 473A
Baskin, A., & Laor, A. 2005, MNRAS, 356, 1029B
Becker, R. H., White, R. L., & Helfand, D. J. 1995, ApJ, 450, 559
Bovy, J., Hennawi, J. F., Hogg, D. W., et al. 2011, ApJ, 729, 141

Boyle, B. J., Shanks, T., Croom, S. M., et al. 2000, MNRAS, 317, 1014
Casali, M., Adamson, A., Alves de Oliveira, C., et al. 2007, A&A, 467, 777
Chiu, K., Richards, G. T., Hewett, P. C., & Maddox, N. 2007, MNRAS, 375, 1180
Condon, J. J., Cotton, W. D., Greisen, E. W., et al. 1998, AJ, 115, 1693
Croom, S. M., Warren, S. J., & Glazebrook, K. 2001, MNRAS, 328, 150
Cui, X.-Q., Zhao, Y.-H., Chu, Y.-Q., et al. 2012, RAA, 12, 1197
Cutri, R. M., et al. 2012, VizieR On-line Data Catalog, 2311, 0
Dong, X.-B., Wang, T.-G., Wang, J.-G., et al. 2008, MNRAS, 383, 581
Fan, X. 1999, AJ, 117, 2528
Fan, X., White, R. L., Davis, M., et al. 2000, AJ, 120, 1167
Fitzpatrick, E. L. 1999, PASP, 111, 63
Graham, M. J., Djorgovski, S. G., Drake, A. J., et al. 2014, MNRAS, 439, 703G
Greene, J. E., & Ho, L. C. 2005a, ApJ, 627, 721
Greene, J. E., & Ho, L. C. 2005b, ApJ, 630, 122
Hambly, N., Collins, R. S., Cross, N. J. G., et al. 2008, MNRAS, 384, 637
Hennawi, J. F., & Prochaska, J. X. 2007, ApJ, 655, 735H
Hewett, P. C., Warren, S. J., Leggett, S. K., & Hodgkin, S. T. 2006, MNRAS, 367, 454
Ho, L. C., Goldoni, P., Dong, X.-B., Greene, J. E., & Ponti, G. 2012, ApJ, 754, 11
Huo, Z.-Y., Liu, X.-W., Liu, X., et al. 2013, AJ, 145, 159
Kirkpatrick, J. A., Schlegel, D. J., Ross, N. P., et al. 2011, ApJ, 743, 125
Kollmeier, J. A., Onken, C. A., Kochanek, C. S., et al. 2006, ApJ, 648, 128
Komossa, S., Xu, D., Zhou, H., Storchi-Bergmann, T., & Binette, L. 2008, ApJ, 680, 926
Laor, A., Jannuzi, B. T., Green, R. F., & Boroson, T. A. 1997, ApJ, 489, 656
Lawrence, A., Warren, S. J., Almaini, O., et al. 2007, MNRAS, 379, 1599
Luo, A.-L., Zhang, H.-T., Zhao, Y.-H., et al. 2012, RAA, 12, 1243
Luo, A.-Li, Zhao, Yong-Heng, Zhao, G., et al. 2015, RAA, 15, 1095
MacLeod, C. L., Brooks, K., Ivezić, Ž., et al. 2011, ApJ, 728, 26
Maddox, N., Hewett, P. C., Péroux, C., Nestor, D. B., & Wisotzki, L. 2012, MNRAS, 424, 2876
Maddox, N., Hewett, P. C., Warren, S. J., & Croom, S. M. 2008, MNRAS, 386, 1605
Markwardt, C. B. 2009, in ASP Conf. Ser. 411, Astronomical Data Analysis Software and Systems XVIII, ed. D. A. Bohlender, D. Daniel, & P. Dowler (San Francisco, CA: ASP), 251
McLure, R. J., & Dunlop, J. S. 2004, MNRAS, 352, 1390
Morganson, E., Burgett, W. S., Chambers, K. C., et al. 2014, ApJ, 784, 92M
Mortlock, D. J., Warren, S. J., Venemans, B. P., et al. 2011, Natur, 474, 616M

Palanque-Delabrouille, N., Yeche, Ch., Myers, A. D., et al. 2011, A&A, 530, 122
Pâris, I., Petitjean, P., Aubourg, É., et al. 2012, A&A, 548, 66
Peng, N., Zhang, Y., Zhao, Y., & Wu, X.-b. 2012, MNRAS, 425, 2599
Richards, G. T., Fan, X., Newberg, H. J., et al. 2002, AJ, 123, 2945
Richards, G. T., Myers, A. D., Gray, A. G., et al. 2009, ApJS, 180, 67
Richards, G. T., Nichol, R. C., Gray, A. G., et al. 2004, ApJS, 155, 257
Richards, G. T., Strauss, M. A., Fan, X., et al. 2006, AJ, 131, 2766
Ross, N. P., Shen, Y., Strauss, M. A., et al. 2009, ApJ, 697, 1634R
Ross, N. P., Myers, A. D., Sheldon, E. S., et al. 2012, ApJS, 199, 3
Salviander, S., Shields, G. A., Gebhardt, K., & Bonning, E. W. 2007, ApJ, 662, 131
Schlegel, D. J., Finkbeiner, D. P., & Davis, M. 1998, ApJ, 500, 525
Schmidt, M. 1963, Natur, 197, 1040
Schneider, D. P., Hall, P. B., Richards, G. T., et al. 2007, AJ, 134, 102
Sharp, R. G., Sabbey, C. N., Vivas, A. K., et al. 2002, MNRAS, 337, 1153
Shen, Y., Richards, G. T., Strauss, M. A., et al. 2011, ApJS, 194, 45
Smail, I., Sharp, R., Swinbank, A. M., et al. 2008, MNRAS, 389, 407
Smith, J. R., Croom, S. M., Boyle, B. J., et al. 2005, MNRAS, 359, 57
Tsuzuki, Y., Kawara, K., Yoshii, Y., et al. 2006, ApJ, 650, 57
Vanden Berk, D. E., Richards, G. T., Bauer, A., et al. 2001, AJ, 122, 549
Vanden Berk, D. E., Wilhite, B. C., Kron, R. G., et al. 2004, ApJ, 601, 692
van der Marel, R. P., & Franx, M. 1993, ApJ, 407, 525
Véron-Cetty, M.-P., Joly, M., & Véron, P. 2004, A&A, 417, 515
Vestergaard, M., & Peterson, B. M. 2006, ApJ, 641, 689
Wang, F., Wu, X.-B., Xiaohui, F., et al. 2015, ApJL, 807, L9
Wang, J.-G., Dong, X.-B., Want, T.-G., et al. 2009a, ApJ, 707, 1334
Wang, J.-M., Chen, Y.-M., Hu, C., et al. 2009b, ApJ, 705, 76
Warren, S. J., Hewett, P. C., & Fsoltz, C. B. 2000, MNRAS, 312, 827
Wright, E. L., Eisenhardt, P. R. M., Mainzer, A. K., et al. 2010, AJ, 140, 1868
Wu, X.-B., Hao, G., Jia, Z., Zhang, Y., & Peng, N. 2012, AJ, 144, 49
Wu, X.-B., & Jia, Z. 2010, MNRAS, 406, 1583
Wu, X.-B., Wang, R., Schmidt, K. B., et al. 2011, AJ, 142, 78
Wu, X.-B., Chen, Z.-Y, Jia, Z.-D, et al. 2010, RAA, 10, 8
Wu, X.-B., Wang, F., Fan, X., et al. 2015, Natur., 518, 512
Yèche, Ch., Petitjean, P., Rich, J., et al. 2010, A&A, 523, 14
Yi, W.-M., Wang, F., Wu, X.-B, et al. 2014, ApJL, 795, L29
Yuan, H., Zhang, H., Zhang, Y., et al. 2013, A&C, 3, 65
Zhao, G., Zhao, Y. H., Chu, Y. Q., et al. 2012, RAA, 12, 723
Zuo, W., Wu, X.-B., Fan, X., et al. 2015, ApJ, 799, 189
Zuo, W., Wu, X.-B., Liu, Y.-Q., & Jiao, C.-L. 2012, ApJ, 758, 104